Shock and Vibration 20 (2013) 1073–1092
DOI 10.3233/SAV-130823
IOS Press

Influence of axial loads on the nonplanar vibrations of cantilever beams

Eulher C. Carvalho[a], Paulo B. Gonçalves[a,*], Giuseppe Rega[b] and Zenón J.G.N. Del Prado[c]
[a]*Pontifical Catholic University of Rio de Janeiro, Rio de Janeiro, RJ, Brazil*
[b]*Sapienza University of Rome, Rome, Italy*
[c]*Federal University of Goiás, Goiânia, GO, Brazil*

Abstract. In this paper an inextensible cantilever beam subject to a concentrated axial load and a lateral harmonic excitation is investigated. Special attention is given to the effect of the axial load on the frequency-amplitude relation, bifurcations and instabilities of the beam. To this aim, the nonlinear integro-differential equations describing the flexural-flexural-torsional coupling of the beam are used, together with the Galerkin method, to obtain a set of discretized equations of motion, which are in turn solved by using the Runge-Kutta method. Both inertial and geometric nonlinearities are considered in the present analysis. Due to symmetries of the beam cross section, the beam exhibits a 1:1 internal resonance which has an important role on the nonlinear oscillations and bifurcation scenario. The results show that the axial load influences the stiffness of the beam changing its nonlinear behavior from hardening to softening. A detailed parametric analysis using several tools of nonlinear dynamics unveils the complex dynamic behavior of the beam in the parametric and external resonance regions. Bifurcations leading to multiple coexisting solutions are observed.

Keywords: Flexural-flexural-torsional coupling, cantilever beam, axial load, bifurcation analysis, parametric instability, nonplanar vibrations

1. Introduction

Highly flexible beams, such as self-supporting towers, columns, pipes, chimneys, masts of cable-stayed towers, risers used in the offshore industry, satellite antennas, micro and nano beams, solar panels in spacecraft stations, robot arms and long-span bridges can, when excited, exhibit large displacements, as well as nonplanar motions, leading to various types of bifurcations, coexistence of different solutions and dynamic jumps, which lead to sudden changes in the state of stress and strain of the structure.

To correctly describe the dynamic characteristics of slender beams, it is necessary to consider in the equations of motion both geometric and inertial nonlinearities. In 1978 Crespo da Silva and Glynn [1,2] derived a set of equations of motion considering the three-dimensional motions of an inextensible beam and including both nonlinearities. The formulation considers flexural motions in two orthogonal planes and torsional vibrations. When the torsional stiffness is much higher than the flexural stiffnesses the formulation is reduced to two equations of motion, considering only the two transversal displacements. Due to its high accuracy, their formulation was the basis for several investigations in the past decades, encompassing various aspects intrinsic to the nonlinear nonplanar behavior of slender beams.

Crespo da Silva and Glynn [3], for example, using the two bending equations presented in the previous work, studied by a perturbation method the three-dimensional oscillations of a beam with symmetric boundary conditions

*Corresponding author: Paulo B. Gonçalves, Pontifical Catholic University of Rio de Janeiro, Rua Marquês de São Vicente 225, Rio de Janeiro, RJ, Brazil. Tel.: +55 21 3527 1189; E-mail: paulo@puc-rio.br.

ISSN 1070-9622/13/$27.50

under planar distributed harmonic excitation. In another paper, Crespo da Silva and Glynn [4] studied the nonlinear response of a beam with asymmetric support conditions. Later, Crespo da Silva and Zaretzky [5], using now three integro-differential equations of motion, studied the flexural-flexural-torsional coupled motion of cantilever beams. The beam was subjected to an in-plane resonant bending excitation in the presence of a one-to-one internal resonance between the third in-plane flexural eigenfrequency and the fundamental torsional frequency. In the same year, Zaretzky and Crespo da Silva [6] investigated experimentally the coupled nonlinear nonplanar motions of a clamped-free beam under a harmonic transverse base excitation.

Pai and Nayfeh [7], using the Galerkin method and perturbation techniques, studied the flexural-torsional oscillations of an inextensional clamped-clamped beam subject to distributed harmonic load. The nonplanar motion of a cantilever beam under lateral harmonic base excitation was also studied by Pai and Nayfeh [8]. Some years later, Pai and Nayfeh [9–11] formulated equations of motion similar to those derived by Crespo da Silva and Glynn [1,2] for the study of composite beams.

Cusumano and Moon [12,13] investigated the nonlinear dynamic behavior of an externally excited thin elastica. The authors conducted an experimental study of the coupled motions of a beam with a slender rectangular cross-section and proposed a simplified two-degree-of-freedom model for its analysis. Chaotic motion involving flexural-torsional coupling was detected. Hamdan et al. [14], using the method of multiple scales, studied the parametric instability and nonplanar response of a flexible cantilever beam under vertical harmonic base excitation. Malatkar and Nayfeh [15] conducted a theoretical and experimental study of the nonlinear planar oscillations of a metallic flexible cantilever beam subject to an external harmonic excitation with a frequency near to the third natural frequency of the beam. Energy transfer between widely spaced modes was observed. Siddiqui et al. [16] analyzed the large amplitude motions of a cantilever beam carrying a moving mass. Di Egidio et al. [17,18] developed a nonlinear formulation and studied the forced vibrations of an inextensible cantilever beams with open cross section. A review of the main contributions in this area up to 2004 can be found in the book by Nayfeh and Pai [19]. Examples of more recent research on the dynamics of free-clamped beams can be found in [20–24]. These studies employ the equations of motion formulated by Crespo da Silva and Glynn [1,2].

As observed above, the nonlinear dynamics of inextensible flexible cantilever beams has been extensively studied in the past, but without taking into account the effect of axial loads, which is important for applications in several engineering branches. Among the few studies on this subject, Arafat et al. [25] showed that the equations formulated by Crespo da Silva and Glynn [1,2] can be used to study the coupled motion of cantilever beams axially excited by a base vibration. Zhang et al. [26] presented the analysis of the global bifurcations and chaotic dynamics for the nonlinear nonplanar oscillations of a cantilever beam subjected to a harmonic axial excitation and transverse excitation at the free end. Using the Galerkin procedure and the method of multiple scales, the authors studied several types of internal resonances and the existence of chaotic motions.

This paper aims at studying the relative influence of static plus harmonic axial loads on the flexural-flexural-torsional coupled motion of inextensible very slender cantilever beams. Special attention is given to the effect of axial load on the frequency-amplitude relation, bifurcations and instabilities of the beam. Due to symmetries of the beam cross section, this investigation focuses on the 1:1 internal resonance which has an important role in the nonlinear oscillations and bifurcation scenario. The Galerkin procedure is applied to obtain a three-degree-of-freedom nonlinear system which is in turn solved by using the Runge-Kutta method. The results show that the axial load influences the stiffness of the beam changing its nonlinear behavior from hardening to softening. A detailed parametric analysis using several tools of nonlinear dynamics unveils the complex dynamic behavior of the beam in the parametric and external resonance regions.

2. Dynamic system

A uniform, homogeneous, inextensible and initially straight beam of isotropic linear elastic material, length L and mass m per unit length is considered in this paper. A deformed beam segment of length s is shown in Fig. 1, where the axes X, Y and Z define the inertial rectangular coordinate system, while ξ, η and, ζ denote a local orthogonal curvilinear coordinate system of the beam at arc length s in the deformed configuration, which coincides with the principal axes of the beam cross section. In the undeformed configuration, the ξ and X axes are coincident and

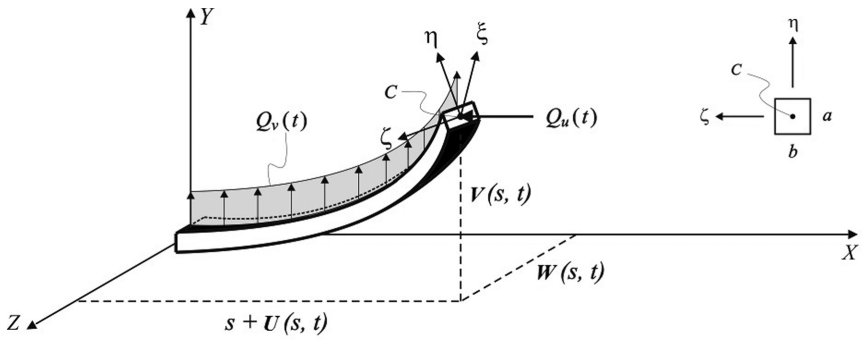

Fig. 1. Coordinate systems, displacements, loading and beam cross section.

the η and ζ axes are parallel to Y and Z, respectively. To investigate the relative influence of an axial load on the nonlinear dynamic behavior of slender cantilever beams, a beam with constant rectangular cross section with height a and width b is adopted, as shown in Fig. 1. The beam is subjected to an axial concentrated load applied at the free end of the beam and given by $Q_u(t) = P_s + q_u \cos(\Omega_u t)$, where P_s is the static load and $q_u \cos(\Omega_u t)$ is a harmonic excitation with frequency Ω_u, magnitude q_u and t is the time. In the Y direction a uniformly distributed lateral harmonic excitation defined by $Q_v(t) = q_v \cos(\Omega_v t)$ is considered, where q_v is the excitation magnitude and Ω_v the excitation frequency.

3. Equations of motion

The nonlinear third-order PDEs equations governing the three-dimensional motion of the beam are:

$$
\begin{aligned}
&m\ddot{V} + c_v\dot{V} + \beta_y(D_\eta V'')'' + [P_s + q_u\cos(\Omega_u t)]\,V'' = \Bigg\{ - D_\eta\beta_\gamma\Gamma' W'' + D_\eta\,(1-\beta_y) \\
&\left[(W''\Gamma)' - \left(\Gamma^2 V''\right)' + W'''\int_0^s V'W''ds\right] - D_\eta\beta_y V'\left(V''^2 + W''^2\right) + V'\Bigg[-D_\eta\beta_y V'V''' - \\
&D_\eta W'W''' + J_\zeta\ddot{V}'V' + J_\eta\ddot{W}'W' - \frac{1}{2}m\int_L^s\int_0^s\left(V'^2 + W'^2\right)^{\bullet\bullet} dsds\Bigg] + J_\xi\Bigg[\dot{\Gamma} + \int_0^s (V'W'')^{\bullet} ds - \\
&\dot{W}'V'\Bigg]\dot{W}' + \left[(J_\eta - J_\zeta)\left(\dot{V}'\Gamma^2 + \dot{W}'\Gamma - \dot{W}'\int_0^s V'W''ds\right) + J_\zeta\dot{V}'\right]^{\bullet} + V'\left(J_\zeta\dot{V}'^2 + J_\eta\dot{W}'^2\right) - \\
&J_\xi c_\gamma W'\dot{\Gamma}\Bigg\}' - [P_s + q_u\cos(\Omega_u t)]\left[V'\left(V'^2 + W'^2\right)\right]' + q_v\cos(\Omega_v t)\,,
\end{aligned}
\tag{1}
$$

$$
\begin{aligned}
&m\ddot{W} + c_w\dot{W} + (D_\eta W'') + [P_s + q_u\cos(\Omega_u t)]\,W'' = \{D_\eta\beta_\gamma\Gamma' V'' + D_\eta\,(1-\beta_y) \\
&\left[(W''\Gamma)' + \left(\Gamma^2 W''\right)' - V'''\int_0^s V''W'ds\right] - D_\eta W'\left(V''^2 + W''^2\right) + W'\Bigg[-D_\eta\beta_y V'V''' - \\
&D_\eta W'W''' + J_\zeta\ddot{V}'V' + J_\eta\ddot{W}'W' - \frac{1}{2}m\int_L^s\int_0^s\left(V'^2 + W'^2\right)^{\bullet\bullet} dsds\Bigg] - J_\xi\Bigg[\dot{\Gamma} + \int_0^s (V'W'')^{\bullet} ds - \\
&\dot{W}'V'\Bigg]\dot{V}' - \left[(J_\eta - J_\zeta)\left(\dot{W}'\Gamma^2 + \dot{V}'\Gamma - \dot{V}'\int_0^s V''W'ds\right) - J_\eta\dot{W}'\right]^{\bullet} + W'\left(J_\zeta\dot{V}'^2 + J_\eta\dot{W}'^2\right)\Bigg\}' - \\
&[P_s + q_u\cos(\Omega_u t)]\left[W'\left(V'^2 + W'^2\right)\right]',
\end{aligned}
\tag{2}
$$

$$J_\xi \ddot{\Gamma} + J_\xi c_\gamma \dot{\Gamma} - D_\eta \beta_\gamma \Gamma'' = -D_\eta \left(1-\beta_y\right)\left[\left(V''^2 - W''^2\right)\Gamma - V''W''\right] - \\ J_\xi \left[\int_0^s \left(V'W''\right)^\bullet ds - V'\dot{W}'\right]^\bullet + \left(J_\eta - J_\zeta\right)\left[\left(\dot{V}'^2 - \dot{W}'^2\right)\Gamma - \dot{V}'\dot{W}'\right]. \tag{3}$$

Details of this formulation, not considering the axial load, can be found in Crespo da Silva [27]. The boundary conditions for the cantilever beam are:

$$U(0,t) = V(0,t) = W(0,t) = \Gamma(0,t) = V'(0,t) = W'(0,t) = 0, \\ \Gamma'(L,t) = V''(L,t) = V'''(L,t) = W''(L,t) = W'''(L,t) = 0, \tag{4}$$

where, $\Gamma = \Gamma(s,t)$ is the angle of torsion of the beam given by:

$$\Gamma = \phi + \int_0^s \left(V''W'\right) ds = \phi + V'W' - \int_0^s \left(V'W''\right) ds, \tag{5}$$

with $\phi = \phi(s,t)$ being an angle that describes the orientation of the cross section at location s.

In the above equations $U = U(s,t)$ is the displacement in the X direction while $V = V(s,t)$ and $W = W(s,t)$ are the deflections of the beam in the Y and Z directions, respectively. The superscript $(')$ denotes partial differentiation with respect to s and the superscript $(\cdot)$ means differentiation with respect to time t. The nondimensional parameters $\beta_y = D_\zeta/D_\eta$ and $\beta_\gamma = D_\xi/D_\eta$ are used, too. Finally, c_v, c_w and c_γ, are the linear viscous damping coefficients. For convenience, the Eqs (1)–(3) can be nondimensionalized by introducing the following quantities: $W^* = W/L$, $V^* = V/L$, $s^* = s/L$, $c_v^* = c_v L^2\sqrt{m/D_\eta}$, $c_w^* = c_w L^2\sqrt{m/D_\eta}$, $c_\gamma^* = c_\gamma L^2\sqrt{m/D_\eta}$, $t^* = t\sqrt{D_\eta/mL^4}$, $J_\eta^* = J_\eta/mL^2$, $J_\zeta^* = J_\zeta/mL^2$, $J_\xi^* = J_\eta^* + J_\zeta^*$ and $\Omega^* = \Omega L^2\sqrt{m/D_\eta}$.

4. Eigenfunctions

The approximate solution for the equations of motion of the beam is obtained by applying the Galerkin method to Eqs (1)–(3). Following Crespo da Silva and Zaretzky [5], first the linear eigenfunctions and eigenfrequencies are obtained from the solution of the undamped and unloaded linearized equations of motion. The eigenfunctions are obtained based on the separate variable assumption:

$$V(s,t) = F_v(s)v(t), \\ W(s,t) = F_w(s)w(t), \\ \Gamma(s,t) = F_\gamma(s)\gamma(t). \tag{6}$$

where,

$$F_{v,w} = C_{v,w}\left\{\cosh\left(r_{1,3}s\right) - \cos\left(r_{2,4}s\right) \; - K_{v,w}\left[\sinh\left(r_{1,3}s\right) - \left(r_{1,3}/r_{2,4}\right)\sin\left(r_{2,4}s\right)\right]\right\}, \tag{7}$$

$$F_\gamma = C_\gamma \sin\left[\left(2n-1\right)\left(\pi/2\right)s\right] \quad (n = 1, 2, \ldots). \tag{8}$$

In the Eqs (7) and (8), C_v, C_w and C_γ are the normalized normal amplitudes in each degree of freedom. The quantities r_1 to r_4 are obtained from the solution of the characteristic equation:

$$r_{1,3}^4 + r_{2,4}^4 + 2r_{1,3}^2 r_{2,4}^2 \cosh\left(r_{1,3}\right)\cos\left(r_{2,4}\right) + r_{1,3}r_{2,4}\left(r_{2,4}^2 - r_{1,3}^2\right)\sinh\left(r_{1,3}\right)\sin\left(r_{2,4}\right) = 0, \tag{9}$$

which is obtained by imposing the boundary condition $F_{v,w}''' = 0$ on the Eq. (7). Thus, the quantities r_1 to r_4 are:

$$r_1 = \sqrt{-\frac{J_\zeta\omega_v^2}{2\beta_y} + \sqrt{\left(\frac{J_\zeta\omega_v^2}{2\beta_y}\right)^2 + \frac{\omega_v^2}{\beta_y}}}, \tag{10}$$

$$r_2 = \sqrt{+\frac{J_\zeta \omega_v^2}{2\beta_y} + \sqrt{\left(\frac{J_\zeta \omega_v^2}{2\beta_y}\right)^2 + \frac{\omega_v^2}{\beta_y}}}, \tag{11}$$

$$r_3 = \sqrt{-\frac{J_\eta \omega_w^2}{2} + \sqrt{\left(\frac{J_\eta \omega_w^2}{2}\right)^2 + \omega_w^2}}, \tag{12}$$

$$r_4 = \sqrt{+\frac{J_\eta \omega_w^2}{2} + \sqrt{\left(\frac{J_\eta \omega_w^2}{2}\right)^2 + \omega_w^2}}. \tag{13}$$

and the quantities K_v and K_w are given by:

$$K_{v,w} = \frac{r_{1,3}^2 \cosh(r_{1,3}) + r_{2,4}^2 \cos(r_{2,4})}{r_{1,3}^2 \sinh(r_{1,3}) + r_{1,3} r_{2,4} \sin(r_{2,4})}. \tag{14}$$

The flexural frequencies ω_v and ω_w can be obtained from Eq. (7) while the torsional frequencies ω_γ is obtained by:

$$\omega_\gamma = (2n-1)\left(\frac{\pi}{2}\right)\sqrt{\frac{\beta_\gamma}{J_\xi}} \quad (n = 1, 2, \ldots). \tag{15}$$

Using a one mode approximation, the following ordinary dimensionless differential equations of motion are obtained, where, to simplify the notation, the superscript (*) is omitted:

$$\begin{aligned}
&\left[\int_0^1 F_v^2 ds - J_\zeta \int_0^1 F_v'' F_v ds\right]\ddot{v} + \left[c_v \int_0^1 F_v^2 ds\right]\dot{v} + \left[\beta_y \int_0^1 F_v^{IV} F_v ds + \int_0^1 [P_s + q_u \cos(\Omega_u t)] F_v \right.\\
&\left. F_v'' ds\right] v = \alpha_{v1}\gamma w + \alpha_{v2} v\gamma^2 + \alpha_{v3} v w^2 + \alpha_{v4} v^3 + \alpha_{v5}\left(v^2\right)^{\bullet\bullet} v + \alpha_{v6}\left(w^2\right)^{\bullet\bullet} v + \alpha_{v7} v^2 \ddot{v} + \alpha_{v8} v w \ddot{w} + \alpha_{v9}\\
&\dot{w}\dot{\gamma} + \alpha_{v10} w \dot{v}\dot{w} + \alpha_{v11} v (\dot{w})^2 + \alpha_{v12}\left(\dot{v}\gamma^2\right)^{\bullet} + \alpha_{v13}\gamma\ddot{w} + \alpha_{v14} v (\dot{v})^2 + \alpha_{v15} w\dot{\gamma} + \int_0^1 F_v q_v \cos(\Omega_v t)\, ds,
\end{aligned} \tag{16}$$

$$\begin{aligned}
&\left[\int_0^1 F_w^2 ds - J_\eta \int_0^1 F_w'' F_w ds\right]\ddot{w} + \left[c_w \int_0^1 F_w^2 ds\right]\dot{w} + \left[\beta_y \int_0^1 F_w^{IV} F_w ds + \int_0^1 [P_s + q_u \cos(\Omega_u t)] F_w \right.\\
&\left. F_w'' ds\right] w = \alpha_{w1}\gamma v + \alpha_{w2} w\gamma^2 + \alpha_{w3} w v^2 + \alpha_{w4} w^3 + \alpha_{w5}\left(w^2\right)^{\bullet\bullet} w + \alpha_{w6}\left(v^2\right)^{\bullet\bullet} w + \alpha_{w7} w^2 \ddot{w} +\\
&\alpha_{w8} w v \ddot{v} + \alpha_{w9}\dot{v}\ddot{\gamma} + \alpha_{w10} v\dot{w}\dot{v} + \alpha_{w11} w (\dot{v})^2 + \alpha_{w12}\left(\dot{w}\gamma^2\right)^{\bullet} + \alpha_{w13}\gamma\ddot{v} + \alpha_{w14} w (\dot{w})^2,
\end{aligned} \tag{17}$$

$$\begin{aligned}
&\left[\int_0^1 F_\gamma^2 ds\right]\ddot{\gamma} + \left[c_\gamma \int_0^1 F_\gamma^2 ds\right]\dot{\gamma} - \left[\beta_\gamma \int_0^1 F_\gamma'' F_\gamma ds\right]\gamma = \alpha_{\gamma1}\gamma v^2 + \alpha_{\gamma2}\gamma w^2 + \alpha_{\gamma3} v w\\
&+ \left[\alpha_{\gamma4}(vw)^{\bullet} + \alpha_{\gamma5} v w\right]^{\bullet} + \alpha_{\gamma6}\gamma\dot{v} + \alpha_{\gamma7}\gamma\dot{w} + \alpha_{\gamma8}\dot{v}\dot{w}.
\end{aligned} \tag{18}$$

In the above equations α_{vi}, α_{wi} e $\alpha_{\gamma i}$ $(i = 1, 2, \ldots)$ are the Galerkin coefficients, which are listed in Appendix A. To normalize the frequencies of the structure, the normalized normal amplitudes C_v, C_w and C_γ, that appear in Eqs (7) and (8) are chosen so that:

$$\int_0^1 F_v^2 ds - J_\zeta \int_0^1 F_v'' F_v ds = 1, \tag{19}$$

$$\int_0^1 F_w^2 ds - J_\eta \int_0^1 F_w'' F_w ds = 1, \tag{20}$$

$$\int_0^1 F_\gamma^2 ds = 1. \tag{21}$$

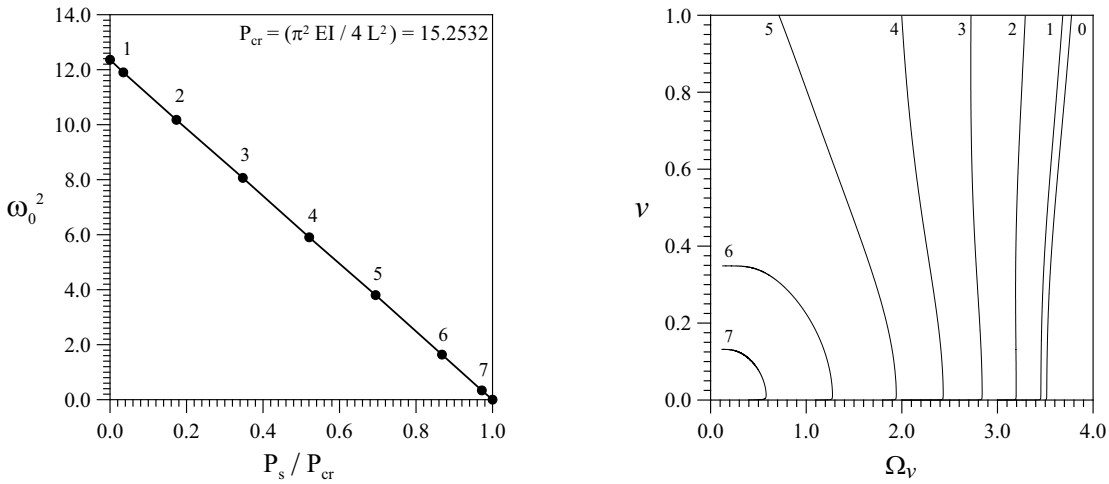

(a) Axial load-frequency relation (b) Frequency-amplitude relations

Fig. 2. Influence of axial static load on the lowest natural frequency and on the nonlinear frequency-amplitude relation.

5. Numerical results

For the numerical analysis, a beam with basic cross section $a/b = 1.0$ (see Fig. 1), length $L = 25b$, non-dimensional distributed moments of inertia $J_\eta = J_\zeta = 0.00013$ and $J_\xi = 0.00026$, non-dimensional parameters $\beta_y = 1.0$ and $\beta_\gamma = 0.64381$, and normalized modal amplitudes $C_v = C_w = 1.0$ and $C_\gamma = 1.4142$, is adopted.

Here, the results are obtained based on the separate variable assumption. In the Section 5.1, the frequency-amplitude relation is obtained, considering only an axial static load $Q_u(s) = P_s$. In Section 5.2, the parametric instability is analyzed, considering only an axial harmonic excitation $Q_u(s) = q_u \cos(\Omega_u t)$ In Section 5.3, the influence of the static load on the parametric instability boundary is studied, considering the axial static load and the axial harmonic excitation $Q_u(s) = P_s + q_u \cos(\Omega_u t)$. Finally, in Section 5.4, the influence of the axial static load on the resonance curve is studied, considering both the static load $Q_u(s) = P_s$ and a lateral harmonic excitation $Q_v(s) = q_v \cos(\Omega_v t)$.

5.1. Influence of the static axial load on the frequency-amplitude relation

With the given parameter values, the system of nonlinear ordinary differential equations is obtained.

$$\begin{cases} \ddot{v} + c_v\dot{v} + (12.3638 + 0.8584P_s + 0.8584q_u\cos(\Omega_u t))\, v - 6.5985\gamma w + \big(22.2693vw^2 \\ +4.3116v^3\big)\left[P_s + q_u\cos(\Omega_u t)\right] + 40.4527\left(vw^2 + v^3\right) + 4.5979\left(\dot{v}^2 + \dot{w}^2 + v\ddot{v} + w\ddot{w}\right) v \\ -1.7246.10^{-3}\left(v^2\ddot{v} + vw\ddot{w} + w\dot{w}\dot{v} + v\dot{v}^2\right) - 6.5005.10^{-4}\dot{w}\dot{\gamma} + 3.2552.10^{-5}w\dot{\gamma} \\ -0.7830q_v\cos(\Omega_v t) = 0 \\ \ddot{w} + c_w\dot{w} + [12.3638 + 0.8584P_s + 0.8584q_u\cos(\Omega_u t)]\, w + 6.5985\gamma v + \big(22.2693wv^2 \\ +4.3116w^3\big)\left[P_s + q_u\cos(\Omega_u t)\right] + 40.4527\left(wv^2 + w^3\right) + 4.5979\left(\dot{w}^2 + \dot{v}^2 + w\ddot{w} + v\ddot{v}\right) w \\ -1.7246.10^{-3}\left(w^2\ddot{w} + vw\ddot{v} + v\dot{v}\dot{w} + w\dot{w}^2\right) + 6.5005.10^{-4}\dot{v}\dot{\gamma} = 0 \\ \ddot{\gamma} + c_\gamma\dot{\gamma} + 5957,0\gamma + 2,6746\left(\ddot{v}w - v\ddot{w}\right) - 0,0001\dot{v}\dot{w} = 0 \end{cases} \tag{22}$$

At first, the damping of the beam is not considered ($c_v = c_w = c_\gamma = 0.0$) and it is assumed $q_v = 10^{-4}$ and $q_u\cos(\Omega_u t) = 0.0$. The lowest natural frequency of the unloaded clamped-free beam is $\omega_0 = 3.5162$, while its critical load is $P_{cr} = (\pi^2 EI/4L^2) = 15.2532$. As the axial load increases the frequency decreases, becoming zero when the axial load reaches the critical value, as illustrated in Fig. 2(a), where the variation of the frequency squared is plotted as a function of the static axial load. The axial load also has a significant influence on the nonlinear

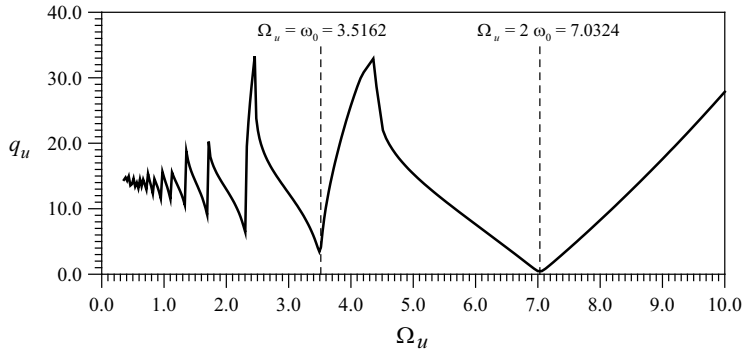

Fig. 3. Parametric instability boundary in the force control space. Axial load: $q_u \cos(\Omega_u t)$.

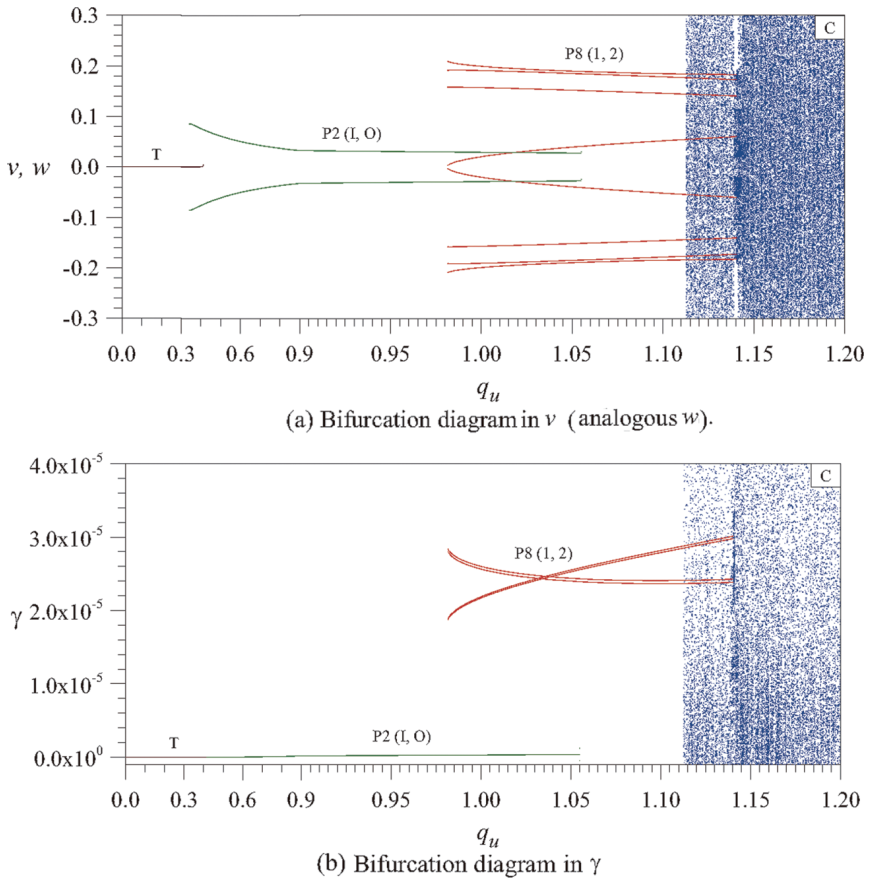

Fig. 4. Bifurcation diagram of the Poincaré map for the beam subject to an axial load at $\Omega_u = 2\omega_0$.

frequency-amplitude relation associated with the lowest natural frequency, as shown in Fig. 2(b). The unloaded beam exhibits a small degree of nonlinearity of the hardening type. As the load increases, first the degree of non-linearity decreases and, at a certain load level, the curve starts to bend to the left (softening behavior) and for high-load levels it exhibits a strong softening nonlinearity.

In bar structures geometric nonlinearities lead to increasing effective stiffness, while inertial nonlinearities lead to a loss of stiffness. This shows that, as the axial load increases, the importance of inertial nonlinearities in the equations of motion also increases. This has been observed experimentally by Jurjo [28].

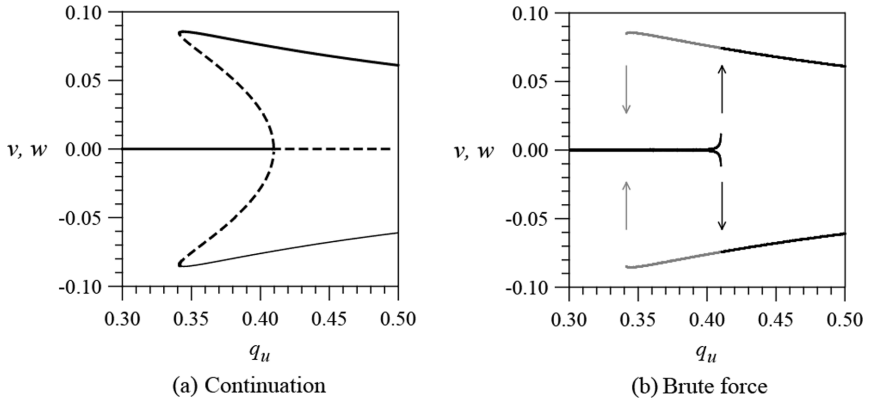

Fig. 5. Bifurcation diagram for $\Omega_u = 2\,\omega_0$ in the vicinity of the parametric instability bifurcation point.

5.2. *Parametric instability at principal and fundamental resonances*

In this section, the nonlinear dynamic behavior of the clamped-free beam subjected only to a harmonic axial load is considered. Here and in the following examples the viscous damping coefficients $c_v = c_w = c_\gamma = 5\%$ are adopted. Figure 3 shows the parametric instability boundary of the beam in the excitation frequency (Ω_u) – excitation magnitude (q_u) control space. It is the threshold beyond which infinitesimal perturbations of the trivial solution result in an initial exponential growth of the lateral oscillations, leading to an oscillatory non-trivial response. The parametric instability boundary is composed of various curves, each one associated with a particular local bifurcation event. The first important instability region is associated with the fundamental resonance zone when the frequency of excitation is equal to the lowest natural frequency (ω_0) of beam lateral vibration. The second V-shaped region to the right is associated with the principal parametric instability region and occurs when the frequency of excitation is equal to two times the lowest natural frequency of the beam ($2\omega_0$). The smaller V-shape regions to the left are related to super-harmonic resonances. As the axial load increases and the natural frequency decreases, the parametric instability boundary moves to the left and approaches zero.

To understand the loss of stability of the beam and the bifurcations associated with the instability boundary, a study of the three-dimensional motions of the beam in the two major regions of parametric instability ($\Omega_u = 2\omega_0$ and $\Omega_u = \omega_0$) is carried out. As a starting point, Fig. 4 displays the bifurcation diagram for $\Omega_u = 2\omega_0$. This bifurcation diagram is obtained by using the brute force algorithm [29] and by taking the magnitude of the axial excitation q_u as the control parameter. Figure 4(a) shows the variation of the fixed points of the Poincaré map for the transversal displacements v and w, which are analogous, while Fig. 4(b) shows the results for the angle of torsion γ. In the figures, six kinds of solution are identified: the trivial solution identified as T solution (brown branch), two coupled non-trivial period two solutions identified as P2 (I, O) (green branch) which, due to the modal coupling and symmetry of the structure, are superimposed in Fig. 4, two coupled non-trivial solutions with period eight identified as P8 (1, 2) (red branch) which also are superimposed in Fig. 4, and the chaotic solution identified as C (blue cloud of points).

Figure 5 shows a detail of the bifurcation diagram in the vicinity of the parametric instability boundary obtained by using continuation techniques [30], Fig. 5(a), and by the brute force method, Fig. 5(b). As the load increases, the trivial solution becomes unstable at $q_u \approx 0.409$ due to a subcritical pitchfork bifurcation, and the response jumps onto the stable periodic solutions with a period two times that of the excitation.

The unstable non-trivial branches emerging at the bifurcation point undergo a saddle-node bifurcation associated with the turning point of the unstable post-critical path at $q_u \approx 0.34$. The dynamic jumps due to the bifurcations observed as the load increases (in black) or decreases (in gray) are illustrated in Fig. 5(b). So, between $q_u \approx 0.34$ and $q_u \approx 0.409$, three coexisting periodic solutions are observed, thus the beam response is a function of the initial conditions.

Two time histories and three projections of the phase-space response of these solutions are illustrated in Fig. 6 for $q_u = 0.38$, together with a cross section of the six-dimensional basin of attraction. The two non-trivial solutions

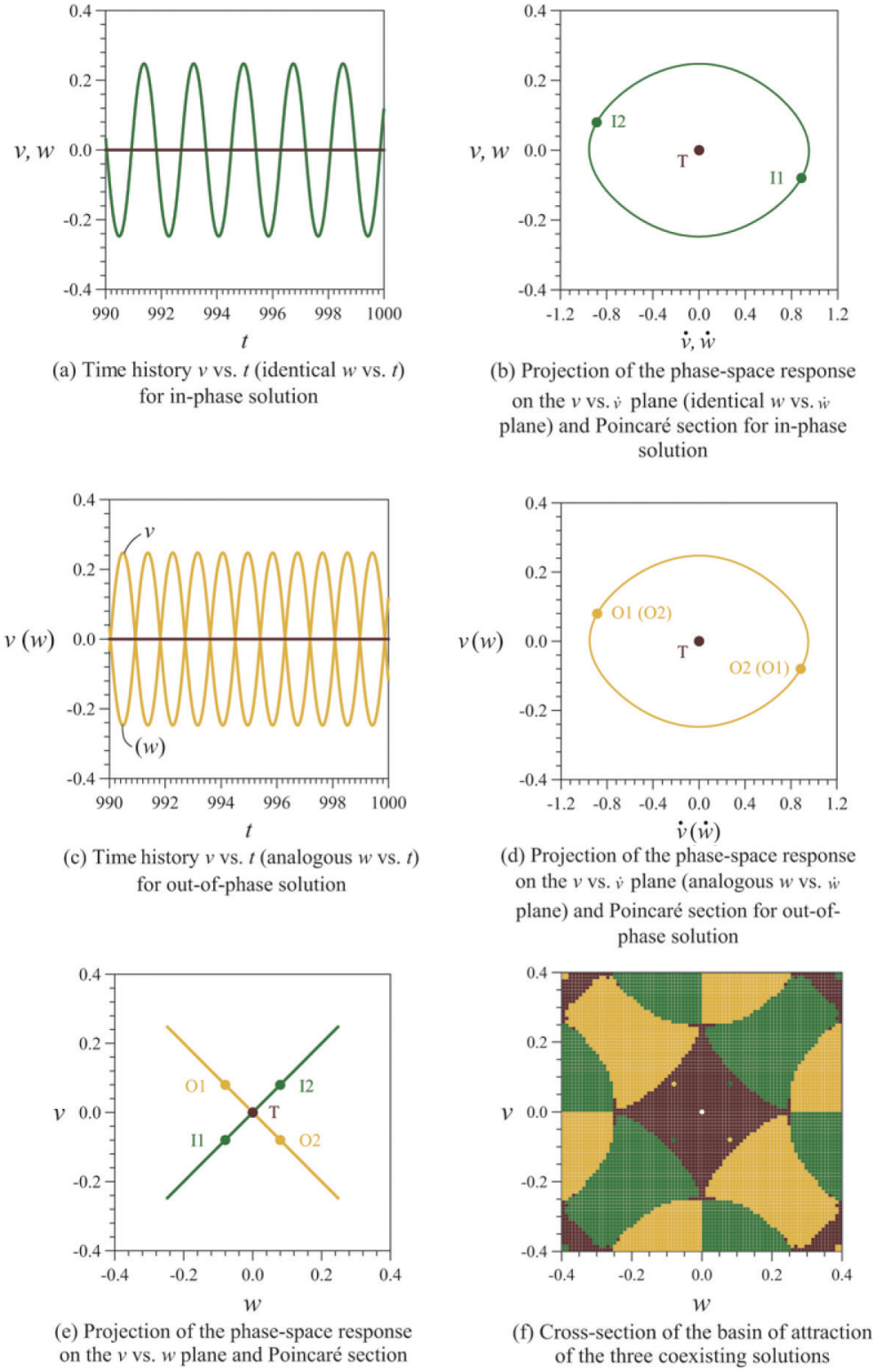

(a) Time history v vs. t (identical w vs. t) for in-phase solution

(b) Projection of the phase-space response on the v vs. $\dot{v}$ plane (identical w vs. $\dot{w}$ plane) and Poincaré section for in-phase solution

(c) Time history v vs. t (analogous w vs. t) for out-of-phase solution

(d) Projection of the phase-space response on the v vs. $\dot{v}$ plane (analogous w vs. $\dot{w}$ plane) and Poincaré section for out-of-phase solution

(e) Projection of the phase-space response on the v vs. w plane and Poincaré section

(f) Cross-section of the basin of attraction of the three coexisting solutions

Fig. 6. Stable coexisting solutions at $q_u = 0.38$ and $\Omega_u = 2\omega_0$.

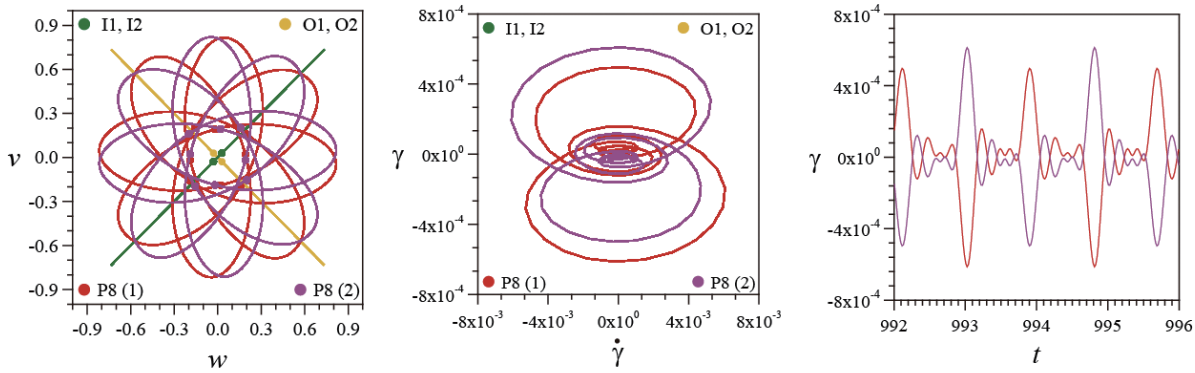

(a) Projection of the phase-space response on the w vs. v plane and Poincaré section

(b) Projection of the phase-space response on the γ vs. $\dot{\gamma}$ plane and Poincaré section

(c) Time history of attractor P8 (1, 2) starting at P8 (1, 2) 1

Fig. 7. Coexisting non-trivial solutions at $q_u = 1.00$ and $\Omega_u = 2\,\omega_0$.

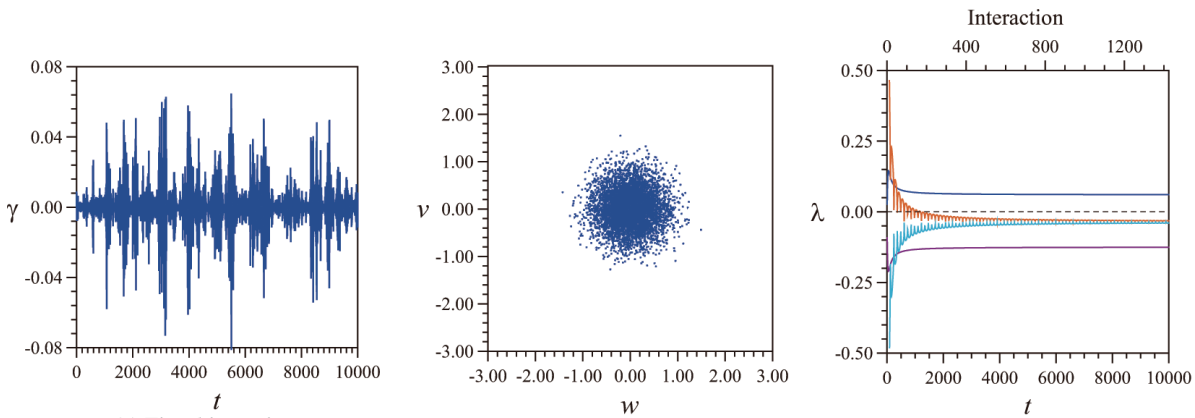

(a) Time history in γ

(b) Projection of Poincaré section

(c) Evolution of the Lyapunov exponents

Fig. 8. Characteristic chaotic response for high forcing magnitudes. $\Omega_u = 2\,\omega_0$ and $q_u = 1.18$.

display the same v and w components, as shown in Figs 6(a) and (c). Solution I (whose green color is used in Figs (4) corresponds to the in-phase response and solution O to the out-of-phase response, as observed in Figs 6(b) and 6(d). The symmetries of the basin of attraction shown in Fig. 6(f) express the underlying symmetries of the structure. In this cross-section (where all remaining phase-space variables are zero) three distinct regions are observed: brown region associated with the trivial solution (white fixed point T), the green region associated with the in-phase non-trivial solution I (fixed points I1 and I2) and yellow region associated with the out-of-phase non-trivial solution O (fixed points O1 and O2). Note that the fixed points of the nontrivial solutions in Fig. 6(f) do not actually belong to the brown six-dimensional basin of attraction, since they are a projection on the considered cross-section. As shown in Fig. 4(b), the angle of torsion for these solutions is zero, the motion occurring at $\pm\,45°$ (see Fig. 6(e)) with v and w exhibiting the same temporal variation.

Increasing the excitation magnitude beyond the parametric instability bifurcation point, a new bifurcation is observed at $q_u \approx 0.981$, where the angle of torsion becomes non-zero ($\gamma \neq 0.0$), as observed in Fig. 4(b). This leads to the appearance of two period eight solutions, called P8 (1) and P8 (2), which corresponds to a coupled flexural-flexural-torsional motion, coexisting with the previous period two solutions, i.e. P2 (I) and P2 (O). The two non-trivial period two solutions disappear at $q_u \approx 1.055$. At $q_u \approx 1.113$ a chaotic solution appears (C), coexisting with the period eight solutions, which disappears for $q_u \geqslant 1.141$. After this load level, only the chaotic response remains.

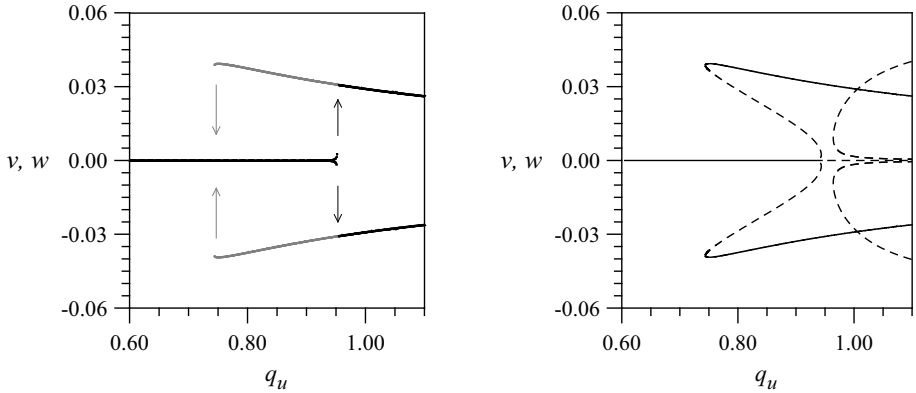

(a) Brute Force (b) Continuation

Fig. 9. Bifurcation diagram for the beam under harmonic axial forcing: $q_u \cos(1.97\omega_0 t)$.

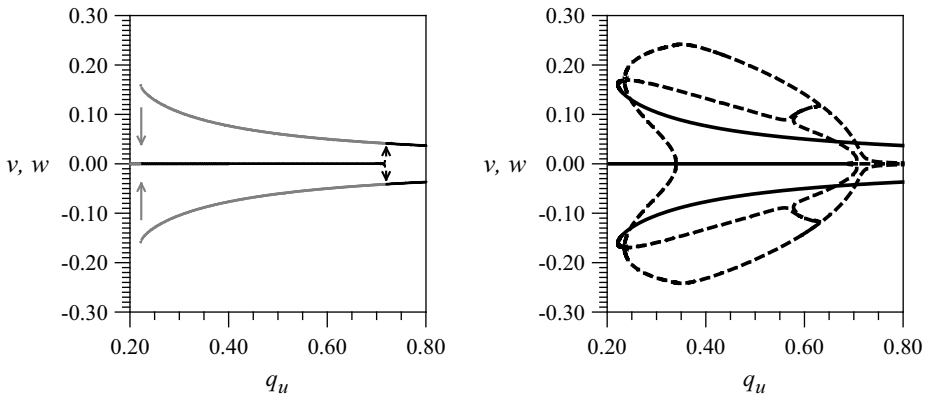

(a) Brute force (b) Continuation

Fig. 10. Bifurcation diagram for the beam under harmonic axial forcing: $q_u \cos(2.02\omega_0 t)$.

Figure 7 shows the four coexisting non-trivial stable solutions at $q_u = 1.00$. Figure 7(a) shows the projection of the four phase-space responses onto the v vs. w plane and the respective Poincaré sections, with the fixed points of the Poincaré map symmetrically distributed around the origin. Figure 7(b) shows the projection of the phase-space responses onto the γ vs. $\dot{\gamma}$ plane, where the presence of the torsional vibrations in the attractors P8 (1) and P8 (2) can be observed. Finally, Fig. 7(c) shows the time history of the angle of torsion γ.

As observed in Fig. 7, for $q_u = 1.00$ the maximum displacement is close to unity. As the dimensionless displacements are divided by the column height $L, v = w = 1.0$ is the highest physically admissible displacement for the beam and the approximations which are at the basis of the present formulation are no longer adequate. Note that, compared with the v and w displacement amplitudes, low values of the torsional angle still occurs, due to the considered compact beam section. More meaningful values are of course expected for open sections.

Finally, Fig. 8 presents the time history response and Poincaré sections, along with the evolution of Lyapunov exponents (λ_i, where $i = 1 \ldots 6$) for $q_u = 1.18$. Figure 8(c) shows that at least one of the exponents is positive ($\lambda_i > 0$), characterizing the motion as chaotic.

Figures 9 and 10 show the bifurcation diagrams in the vicinity of $\Omega_u = 2\omega_0$ for, respectively, a forcing frequency associated with the descending and ascending branches of main parametric instability region. In both cases a subcritical pitchfork bifurcation is observed.

Figures 11(a) and (b) show the bifurcation diagram for $\Omega = \omega_0$, which corresponds to the lowest critical load in the secondary (i.e., fundamental) region of parametric instability (see Fig. 3). The trivial solution (T) becomes unstable at $q_u \approx 4.050$.

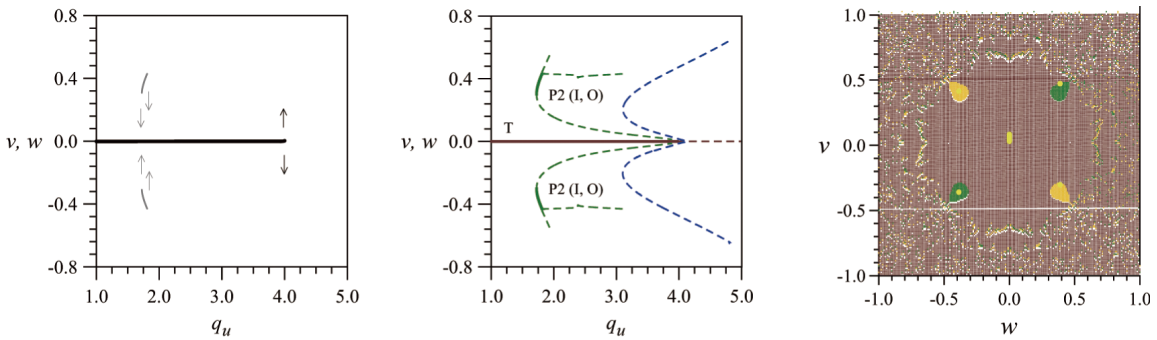

(a) Brute force (b) Continuation (c) Cross-section of the basin of attraction of the three coexisting solutions

Fig. 11. Bifurcation diagram and basin of attraction in the secondary parametric instability region at $\Omega_u = \omega_0$.

Again the beam goes through a subcritical bifurcation, leading to two (in-phase and out-of-phase) period two responses, as shown before. In the bifurcation diagrams, these solutions are superimposed. Thus, between $q_u \approx 1.7255$ and $q_u \approx 1.8095$, three coexisting periodic solutions are observed. Figure 11(c) shows a cross section of the six-dimensional basin of attraction for $q_u = 1.77$. Here, most initial conditions converge to the trivial solution (fixed point T associated with brown basin). Small sets of initial conditions converge to the nontrivial in-phase solution I (green basin) or nontrivial out-of-phase solution O (yellow basin). A high sensitivity is observed varying the initial conditions and sudden changes in vibration patterns are expected, leading to unpredictability.

No stable solutions could be detected after the parametric bifurcation point, as shown in Fig. 11(a), because of the two period two responses being stable in a very narrow range of q_u values. This behavior is particularly dangerous because the structure experiences a definite jump to infinity when the load exceeds the parametric instability boundary, thus leading to the beam's collapse.

5.3. *Influence of the static preload on the parametric instability boundary*

To evaluate the effect of the static preload (P_s) on the parametric instability of the system, the bifurcation diagrams are obtained with the brute force algorithm for increasing static axial load at $\Omega_u = 2\omega_0$, where for each case ω_0 is the lowest natural frequency of the loaded column, as shown in Fig. 2(a). Comparing the bifurcation diagrams in Fig. 12, one observes that, as the static load increases and approaches the critical value, the boundary of parametric instability moves to the left, the parametric critical load decreases and the bifurcations shift from subcritical to supercritical.

The parametric instability boundary for case 3 at principal resonance $\Omega_v = 2\omega_0 (P_s/P_{cr} = 0.35)$ is presented in Fig. 13, along with the reference one in the absence of axial load. Figure 14 shows that for this static load level, subcritical bifurcations are associated with the descending left-side instability boundary, while supercritical bifurcations characterize the ascending right side instability boundary; this is similar to what observed in [31] for a parametrically excited cylindrical shell at principal resonance.

5.4. *Influence of the static preload on the nonlinear response under lateral excitation.*

Next, we investigate the influence of static axial load on the dynamic non-linear behavior of the beam under a distributed lateral harmonic excitation $Q_v(s) = q_v \cos(\Omega_v t)$ at primary resonance $\Omega_v = \omega_0$, applied in the direction of the lateral displacement v (see Fig. 1).

Figure 15 shows the diagrams of bifurcations on the $v - w - \Omega_v$ space for increasing axial static load and considering $q_v = 0.1$. These diagrams are obtained using the continuation software AUTO [32]. Dashed and solid lines refer respectively to the stable and unstable solutions. Here the maximum displacement of the beam is plotted as a function of the excitation frequency. The black curve corresponds to the in-plane vibrations of the beam, where load and structure are contained in the same plane (the displacements w and γ are equal to zero). This corresponds

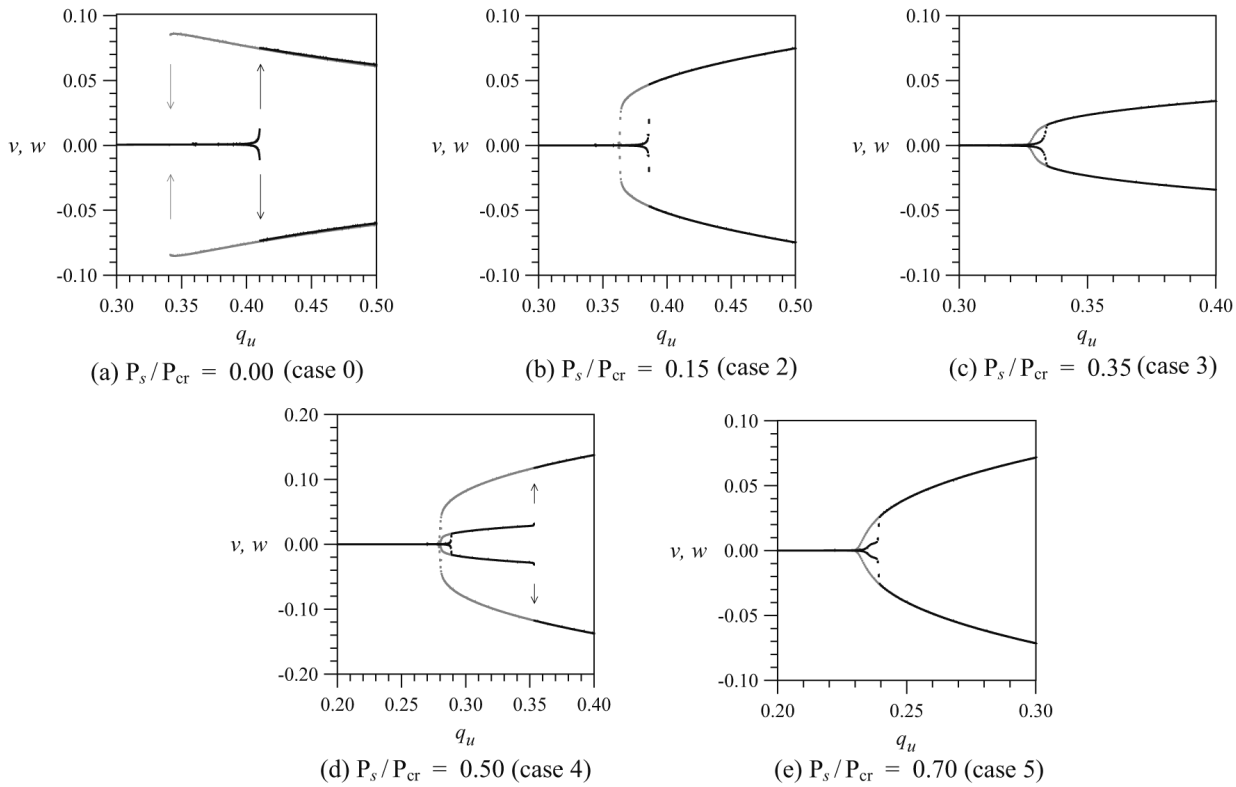

Fig. 12. Bifurcation diagrams of the Poincaré map for the beam subject to increasing static axial load at $\Omega_u = 2\,\omega_0$.

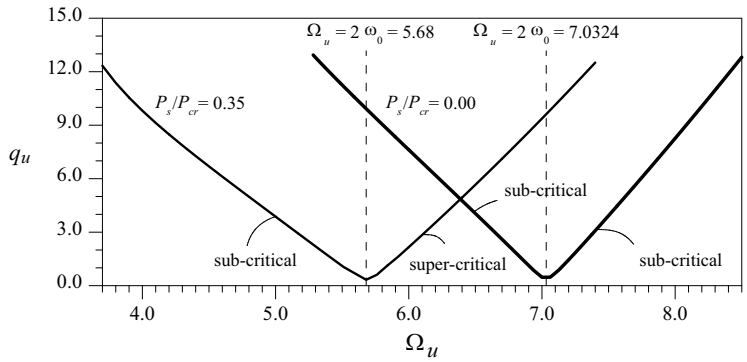

Fig. 13. Parametric instability boundary in the force control space, for an axial static load $P_s/P_{cr} = 0.35$ (case 3).

to the classical resonance curve obtained when the flexural-flexural-torsional coupling is not considered, leading to an erroneous description of the beam oscillations. If only in-plane motions are considered in the structural modeling, only two saddle-node bifurcations occur, which correspond in Fig. 15(a) to the points PF1 and PF2.

When the flexural-flexural-torsional coupling is considered, these saddle-node bifurcations change to unstable pitchfork bifurcations, leading to nonplanar motions (blue and red branches in Fig. 15(a)). Due to the inherent symmetries of the system the two branches of non-planar motions are superimposed in Fig. 15(a). Only a phase difference exists between the two solutions. As expected, they undergo the same sequence of saddle-node bifurcations (SN), leading to a region of stable non-planar motions (between SN1 = SN3 and SN2 = SN4). As the load increases, new bifurcated paths appear, as shown in Figs 15(b)–(c). These bifurcated paths also exhibit several secondary bifurcations.

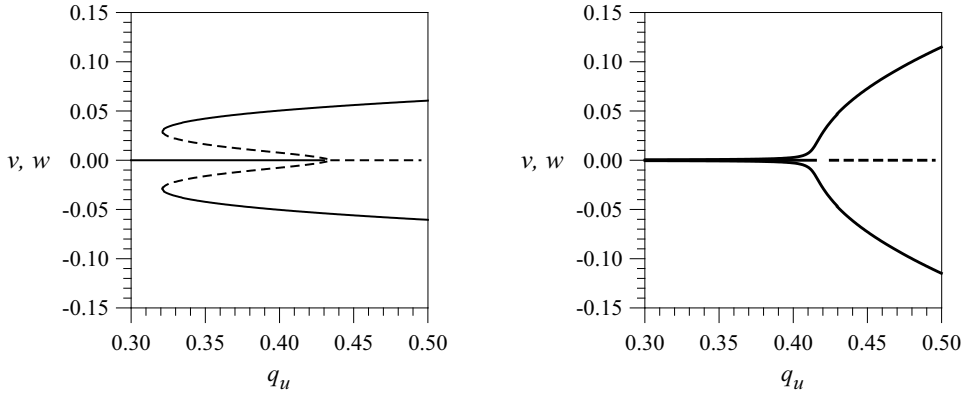

(a) $\Omega_u = 1.98\ \omega_0$ (b) $\Omega_u = 2.02\ \omega_0$

Fig. 14. Characteristic bifurcation diagrams in the principal parametric instability region. $P_s/P_{cr} = 10.35$ (case 3).

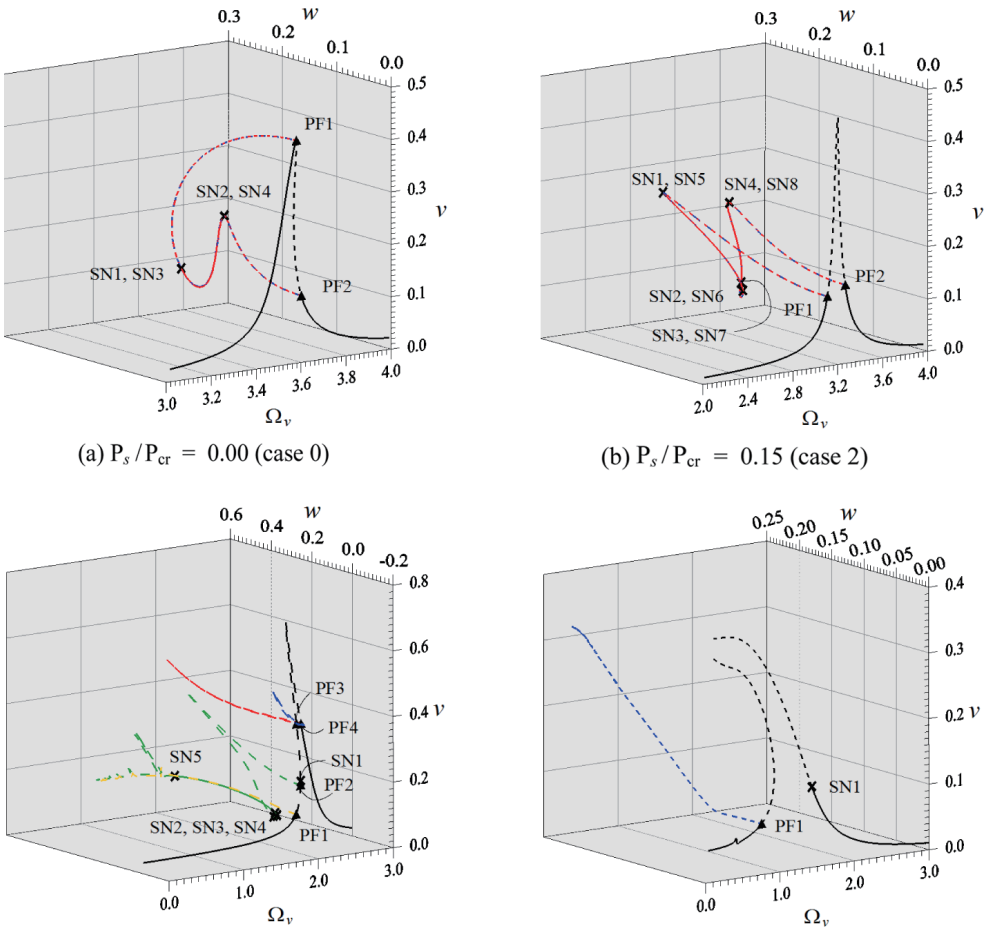

(a) $P_s/P_{cr} = 0.00$ (case 0) (b) $P_s/P_{cr} = 0.15$ (case 2)

(c) $P_s/P_{cr} = 0.50$ (case 4) (d) $P_s/P_{cr} = 0.84$ (case 6)

Fig. 15. Bifurcation diagram in the $v - w - \Omega_v$ space, considering the axial static load and taking the lateral harmonic excitation frequency as control parameter.

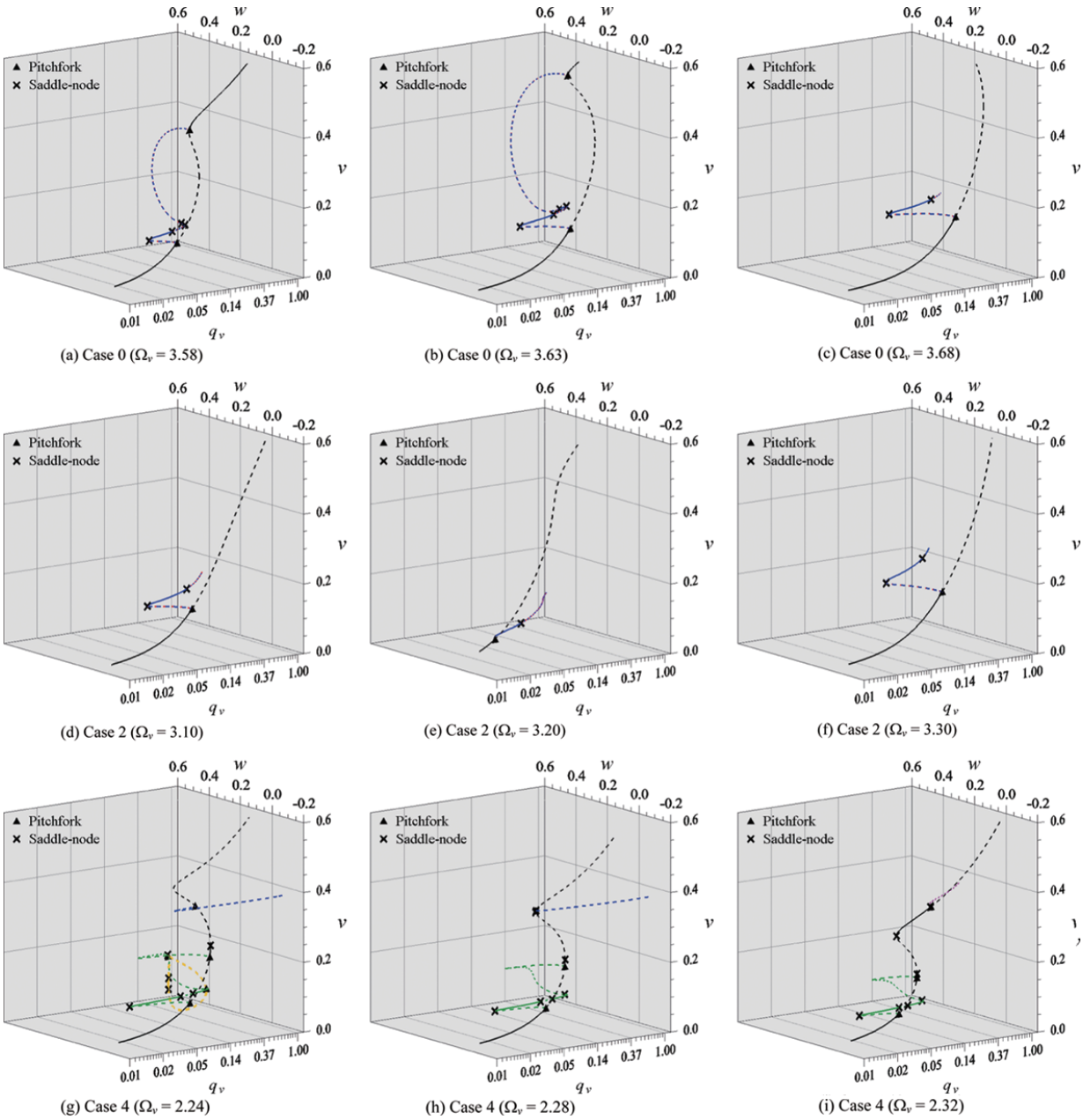

Fig. 16. Bifurcation diagram in the $v - w - q_v$ space, considering an axial static load and taking the lateral harmonic excitation magnitude as control parameter.

For example, in Fig. 15(b) for $P_s/P_{cr} = 0.15$, the pitchfork bifurcation PF1 moves downward along the previously stable resonant branch and new saddle-node bifurcations arise along the bifurcated paths, leading to several planar and non-planar coexisting attractors in some frequency ranges. As the load increases still further and the natural frequency approaches zero, most of the bifurcated paths become unstable and the bifurcation point PF1 moves downwards leading to frequency regions with no stable solutions, as observed in Fig. 15(d). Also, the influence of the load on the backbone curve (see Fig. 2(b)) changes the resonant behavior from hardening to softening.

In addition, Fig. 16 shows the diagrams of bifurcations in the $v - w - q_v$ space for three different values of the lateral excitation frequency and for each of the three axial load magnitudes (i.e. Case 0, Case 2 and Case 4),

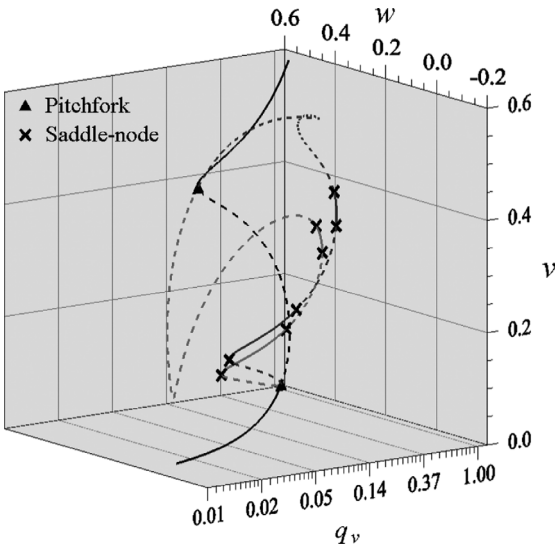

Fig. 17. Bifurcation diagram in the $v - w - q_v$ space, considering a lateral harmonic excitation at 45°. Case 0, $\Omega_v = 3.63$.

associated with the bifurcation diagrams shown in Figs 15(a)–(c). Here the maximum displacement of the beam is plotted as a function of the lateral harmonic excitation magnitude. The colors used to identify the distinct solution branches are the same used in the Fig. 15.

By comparing the results in Fig. 16, we can conclude that the axial static preload has a significant influence on the equilibrium paths and bifurcation sequences. In all cases, as the load increases, the solution becomes unstable due to an unstable pitchfork bifurcation. The bifurcated branches undergo a series of saddle-node bifurcations leading to coexisting stable solutions in some forcing ranges. The two bifurcated branches at the pitchfork bifurcation are coincident, due to the symmetry of the problem. If the beam is excited at a different angle, the two paths emerging at the bifurcation points are distinct, as observed in Fig. 17, where the bifurcation diagram of the unloaded beam excited at 45° is shown.

6. Conclusions

A nonlinear formulation including the geometric and inertial nonlinearities, formulated originally by Crespo da Silva and Glynn [1,2], is considered to investigate the flexural-flexural-torsional response of a cantilever beam subjected to static plus harmonic axial load and possible lateral excitation. Bifurcation diagrams, phase planes and time histories, Poincaré maps, Lyapunov exponents and basins of attraction are used to explore the behavior of the beam in the parametric or external resonance regions. Due to the symmetry of the cross-section, the beam exhibits 1:1 internal resonance.

A detailed bifurcation analysis shows that the axially loaded beam under parametric excitation displays a complex non-linear dynamic behavior with several-coexisting planar and non-planar solutions, and with bifurcation features at parametric instability also depending on the value of the static load. This load has a profound influence on the frequency-amplitude relation and on the resonance curves of the beam under lateral harmonic forcing, leading to an intricate bifurcation scenario and multiplicity of solutions. Also, regions with no stable solutions are detected. So, when designing beams with similar loading conditions, the engineer should be aware of such complex phenomena that may lead to unwanted and even dangerous behavior.

Acknowledgment

The authors gratefully acknowledge the support of FAPERJ, CAPES and CNPq.

Appendix A

The Galerkin coefficients in the Eqs (16)–(18) are defined as follows:

$$\alpha_{v1} = \int_0^1 \left(-\beta_\gamma F_v \left(F_\gamma' F_w''\right)' + (1-\beta_y) F_v \left(F_\gamma F_w''\right)''\right) ds, \tag{A.1}$$

$$\alpha_{v2} = -(1-\beta_y) \int_0^1 \left(F_v \left(F_v'' F_\gamma^2\right)''\right) ds, \tag{A.2}$$

$$\alpha_{v3} = \int_0^1 (1-\beta_y) F_v \left[F_w''' \int_0^s F_v' F_w'' ds\right]' ds - \int_0^1 \beta_y F_v \left(F_v' F_w''^2\right)' ds - \int_0^1 F_v \left(F_v' F_w' F_w'''\right)' ds$$
$$- \int_0^1 P_s + q_u \cos(\Omega_u t) \left(F_v F_w'^2 F_v' + 2 F_v F_v' F_w' F_w''\right) ds, \tag{A.3}$$

$$\alpha_{v4} = -\beta_y \int_0^1 F_v \left[F_v' \left(F_v' F_v''\right)'\right]' ds - \int_0^1 P_s + q_u \cos(\Omega_u t) F_v F_v'^2 F_v'' ds, \tag{A.4}$$

$$\alpha_{v5} = -\frac{1}{2} \int_0^1 F_v \left(F_v' \int_L^s \int_0^s F_v'^2 ds ds\right)' ds, \tag{A.5}$$

$$\alpha_{v6} = -\frac{1}{2} \int_0^1 F_v \left(F_v' \int_L^s \int_0^s F_w'^2 ds ds\right)' ds, \tag{A.6}$$

$$\alpha_{v7} = \alpha_{v14} = J_\zeta \int_0^1 F_v \left(F_v'\right)^{3\prime} ds, \tag{A.7}$$

$$\alpha_{v8} = \int_0^1 \left[J_\eta F_v \left(F_v' F_w'^2\right)' (J_\eta - J_\zeta) F_v \left(F_w' \int_0^s F_v' F_w'' ds\right)'\right] ds, \tag{A.8}$$

$$\alpha_{v9} = 2 J_\eta \int_0^1 F_v \left(F_\gamma F_w'\right)' ds, \tag{A.9}$$

$$\alpha_{v10} = 2 J_\eta \int_0^1 F_v \left(F_w' \int_L^s F_v' F_w'' ds\right)' ds, \tag{A.10}$$

$$\alpha_{v11} = \int_0^1 \left[2 J_\eta F_v \left(F_w' \int_L^s F_v' F_w'' ds\right)' - J_\zeta \int_0^1 F_v \left(F_v' F_w'^2\right)' ds\right] ds, \tag{A.11}$$

$$\alpha_{v12} = (J_\eta - J_\zeta) \int_0^1 F_v \left(F_v' F_\gamma^2\right)' ds, \tag{A.12}$$

$$\alpha_{v13} = (J_\eta - J_\zeta) \int_0^1 F_v \left(F_w' F_\gamma\right)' ds, \tag{A.13}$$

$$\alpha_{v15} = -J_\xi c_\gamma \int_0^1 F_v \left(F_w' F_\gamma\right)' ds, \tag{A.14}$$

$$\alpha_{w1} = \int_0^1 \left(\beta_\gamma F_w \left(F_\gamma' F_v''\right)' + (1-\beta_y) F_w \left(F_\gamma F_v''\right)''\right) ds, \tag{A.15}$$

$$\alpha_{w2} = (1-\beta_y) \int_0^1 \left(F_w \left(F_w'' F_\gamma^2\right)''\right) ds, \tag{A.16}$$

$$\alpha_{w3} = -\int_0^1 (1-\beta_y) F_w \left[F_v''' \int_0^s F_w' F_v'' ds\right]' ds - \int_0^1 F_w \left(F_w' F_v''^2\right)' ds - \int_0^1 \beta_y F_w \left(F_v' F_w' F_v'''\right)' ds$$

$$-\int_0^1 P_s + q_u \cos(\Omega_u t)\left(F_w F_v'^2 F_w' + 2F_w F_w' F_v' F_v''\right) ds, \tag{A.17}$$

$$\alpha_{w4} = -\int_0^1 F_w \left[F_w' \left(F_w' F_w''\right)'\right]' - \int_0^1 P_s + q_u \cos(\Omega_u t) F_w F_w'^2 F_w'' ds, \tag{A.18}$$

$$\alpha_{w5} = -\frac{1}{2}\int_0^1 F_w \left(F_w' \int_L^s \int_0^s F_w'^2 ds ds\right)' ds, \tag{A.19}$$

$$\alpha_{w6} = -\frac{1}{2}\int_0^1 F_w \left(F_w' \int_L^s \int_0^s F_v'^2 ds ds\right)' ds, \tag{A.20}$$

$$\alpha_{w7} = \alpha_{w14} = J_\eta \int_0^1 F_w \left(F_w'\right)^{3\prime} ds, \tag{A.21}$$

$$\alpha_{w8} = \int_0^1 \left[J_\zeta F_w \left(F_w' F_v'^2\right)' + \left(J_\eta - J_\zeta\right) F_w \left(F_v' \int_0^S F_w' F_v'' ds\right)'\right] ds, \tag{A.22}$$

$$\alpha_{w9} = -2J_\eta \int_0^1 F_w \left(F_\gamma F_v'\right)' ds, \tag{A.23}$$

$$\alpha_{w10} = \int_0^1 \left[-J_\xi F_w \left(F_v' \int_L^s F_v' F_w'' ds\right)' + J_\xi \right.$$
$$\left. \int_0^1 F_w \left(F_w' F_v'^2\right)' + (J_\eta - J_\zeta) F_w \left(F_v' \int_L^s F_w' F_v'' ds\right)'\right] ds, \tag{A.24}$$

$$\alpha_{w11} = \int_0^1 \left[-J_\xi F_w \left(F_v' \int_L^s F_v' F_w'' ds\right)' + J_\eta \right.$$
$$\left. \int_0^1 F_w \left(F_w' F_v'^2\right)' + \left(J_\eta - J_\zeta\right) F_w \left(F_v' \int_L^s F_w' F_v'' ds\right)'\right] ds, \tag{A.25}$$

$$\alpha_{w12} = -\left(J_\eta - J_\zeta\right) \int_0^1 F_w \left(F_w' F_\gamma^2\right)' ds, \tag{A.26}$$

$$\alpha_{w13} = -\left(J_\eta - J_\zeta\right) \int_0^1 F_w \left(F_v' F_\gamma\right)' ds, \tag{A.27}$$

$$\alpha_{\gamma 1} = -\frac{1-\beta_y}{J_\xi} \int_0^1 F_\gamma^2 F_v''^2 ds, \tag{A.28}$$

$$\alpha_{\gamma 2} = \frac{1-\beta_y}{J_\xi} \int_0^1 F_\gamma^2 F_w''^2 ds, \tag{A.29}$$

$$\alpha_{\gamma 3} = \frac{1-\beta_y}{J_\xi} \int_0^1 F_\gamma F_w'' F_v'' ds, \tag{A.30}$$

$$\alpha_{\gamma 4} = -\int_0^1 F_\gamma \int_0^s F_v' F_w'' ds ds, \tag{A.31}$$

$$\alpha_{\gamma 5} = \int_0^1 F_\gamma F_v' F_w' ds, \tag{A.32}$$

$$\alpha_{\gamma 6} = \frac{J_\eta - J_\zeta}{J_\xi} \int_0^1 F_v'^2 F_\gamma^2 ds, \tag{A.33}$$

$$\alpha_{\gamma 7} = \frac{-\left(J_\eta - J_\zeta\right)}{J_\xi} \int_0^1 F_w'^2 F_\gamma^2 ds, \tag{A.34}$$

$$\alpha_{\gamma 8} = \frac{-\left(J_\eta - J_\zeta\right)}{J_\xi} \int_0^1 F_\gamma F_v' F_w' ds. \tag{A.35}$$

References

[1] M.R.M. Crespo da Silva and C.C. Glynn, Nonlinear flexural-flexural-torsional dynamics of inextensional beams, I. Equation of motion, *Journal of Structural Mechanics* **6**(4) (1978), 437–448.

[2] M.R.M. Crespo da Silva and C.C. Glynn, Nonlinear flexural-flexural-torsional dynamics of inextensional beams, II. Forced motions, *Journal of Structural Mechanics* **6**(4) (1978), 449–461.

[3] M.R.M. Crespo da Silva and C.C. Glynn, Out-of-plane vibrations of a beam including nonlinear inertia and nonlinear curvature effects, *International Journal of Non-Linear Mechanics* **13** (1979), 261–271.

[4] M.R.M. Crespo da Silva and C.C. Glynn, Nonlinear nonplanar resonant oscillations in fixed-free beams with support asymmetry, *International Journal of Solids and Structures* **15** (1979), 209–219.

[5] M.R.M. Crespo da Silva and C.L. Zaretzky, Nonlinear flexural-flexural-torsional interactions in beams including the effect of torsional dynamics, I. Primary resonance, *Nonlinear Dynamics* **5** (1994), 3–23.

[6] C.L. Zaretzky and M.R.M. Crespo da Silva, Experimental investigation of non-linear modal coupling in the response of cantilever beams, *Journal of Sound and Vibration* **174** (1994), 145–167.

[7] P.F. Pai and A.H. Nayfeh, Non-linear non-planar parametric response of an inextensional beam, *International Journal of Nonlinear Mechanics* **24** (1989), 139–158.

[8] P.F. Pai and A.H. Nayfeh, Non-linear non-planar oscillations of a beam under lateral base excitation, *International Journal of Nonlinear Mechanics* **24** (1991), 455–474.

[9] P.F. Pai and A.H. Nayfeh, Three-dimensional nonlinear vibrations of composite beams. I. Equations of motion, *Nonlinear Dynamics* **1** (1990), 477–502.

[10] P.F. Pai and A.H. Nayfeh, Three-dimensional nonlinear vibrations of composite beams, II. Flapwise excitation, *Nonlinear Dynamics* **2** (1991), 1–34.

[11] P.F. Pai and A.H. Nayfeh, Three-dimensional nonlinear vibrations of composite beams, III. Chordwise excitation, *Nonlinear Dynamics* **2** (1991), 137–156.

[12] J.P. Cusumano and F.C. Moon, Chaotic non-planar vibrations of the thin elastica, part I: Experimental observation of planar instability, *Journal of Sound and Vibration* **179** (1995), 185–208.

[13] J.P. Cusumano and F.C. Moon, Chaotic non-planar vibrations of the thin elastica, part II: Derivation and analysis of a low-dimensional model, *Journal of Sound and Vibration* **179** (1995), 209–226.

[14] M.N. Hamdan, A.A. Qaisia and B.O. Al-Bedoor, Comparison of analytical techniques for nonlinear vibrations of a parametrically excited cantilever, *International Journal of Mechanical Sciences* **43** (2001), 1521–1542.

[15] P. Malatkar and A.H. Nayfeh, On the transfer of energy between widely spaced modes in strictures, *Nonlinear Dynamics* **31** (2003), 225–242.

[16] S.A.Q. Siddiqui, M.F. Golnaraghi and G.R. Heppler, Large free vibrations of a beam carrying a moving mass, *International Journal of Non-Linear Mechanics* **38** (2003), 1481–1493.

[17] A. Di Egidio, A. Luongo and F. Vestroni, A non-linear model for the dynamics of open cross-section thin-walled beams – Part I: Formulation, *International Journal of Nonlinear Mechanics* **38** (2003), 1067–1081.

[18] A. Di Egidio, A. Luongo and F. Vestroni, A non-linear model for the dynamics of open cross-section thin-walled beams – Part II: Forced motion, *International Journal of Nonlinear Mechanics* **38** (2003), 1083–1094.

[19] A.H. Nayfeh and P.F. Pai, Linear and nonlinear structural mechanics, Wiley-VCH, 2004.

[20] W. Zhang, Chaotic motion and its control for nonlinear nonplanar oscillations of a parametrically excited cantilever beam, *Chaos, Solutions and Fractals* **26** (2005), 731–745.

[21] W. Zhang, S. Li and M. Yao, Global bifurcation and manypulse type chaotic dynamics in the nonlinear nonplanar oscillations of a cantilever beam, *Proceedings of the ASME 2009 International Design Engineering Technical Conferences and Computers and Information in Engineering Conference*, San Diego, California (2009).

[22] W.K. Lee, K.S. Lee and C.H. Pak, Stability analysis for nonplanar free vibrations of a cantilever beam by using nonlinear normal modes, *Nonlinear Dynamics* **52** (2008), 217–225.

[23] O. Aghababei, H. Nahvi and S. Ziaei-Rad, Non-linear non-planar vibrations of geometrically imperfect inextensional beams, Part I: Equations of motion and experimental validation, *International Journal of Non-Linear Mechanics* **44** (2009), 147–160.

[24] A. Di Edigio and F. Vestroni, Static behavior and bifurcation of monosymmetric open cross-section thin-walled beam: Numerical and experimental analysis, *International Journal of Solids and Structures* **48** (2011), 1894–1905.

[25] H. Arafat, A.H. Nayfeh and C. Chin, Nonlinear nonplanar dynamics of parametrically excited cantilever beams, *Nonlinear Dynamics* **15** (1998), 31–61.

[26] W. Zhang, F.X. Wang and M.H. Yao, Global bifurcation and chaotic dynamics in nonlinear nonplanar oscillation of a parametrically excited cantilever beam, *Nonlinear Dynamics* **40** (2005), 251–279.

[27] M.R.M. Crespo da Silva, Equations for nonlinear analysis of 3D motions of beams, *Applied Mechanics Reviews* **44** (1991), 51–59.

[28] D.L.B.R. Jurjo, Estabilidade de colunas sujeitas ao peso próprio, *Master thesis – Department of Civil Engineering*, Pontifical Catholic University, Rio de Janeiro, (2001).
[29] A.H. Nayfeh and B. Balachandran, Applied nonlinear dynamics, Analitical, computacional and experimental methods, John Wiley & Sons, Inc., New York, 1995.
[30] E.L. Allgower and G. Kurt, Introduction to numerical continuation methods, John Wiley & Sons, Inc., New York, 1979.
[31] P.B. Gonçalves, F.M.A. Silva, G. Rega and S. Lenci, Global dynamics and integrity of a two-d.o.f. model of a parametrically excited cylindrical shell, *Nonlinear Dynamics* **63** (2011), 61-82.
[32] E.J. Doedel, A.R. Champneys, T.F. Fairgrieve, Y.A. Kuznetsov, B. Sandstede and X. Wang, AUTO 97, Concordia University, Montreal, Canada, 1998.